ACS APPLIED ELECTRONIC MATERIALS

pubs.acs.org/acsaelm Article

Large Damping-like Spin−Orbit Torque and Improved Device Performance Utilizing Mixed-Phase Ta

Akash Kumar, Raghav Sharma, Kacho Imtiyaz Ali Khan, Chandrasekhar Murapaka, Gerard Joseph Lim, Wen Siang Lew, Sujeet Chaudhary, and Pranaba Kishor Muduli*

Cite This: *ACS Appl. Electron. Mater.* 2021, 3, 3139−3146 Read Online

ACCESS | Metrics & More | Article Recommendations | Supporting Information

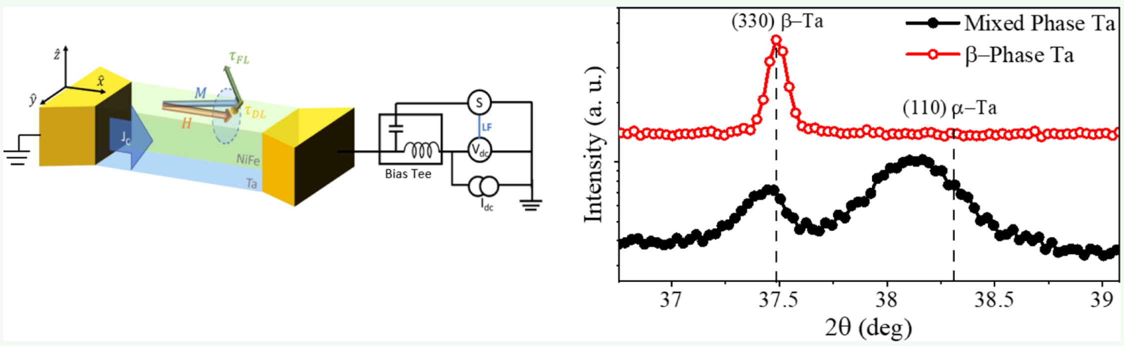

ABSTRACT: The β phase of Ta is known to exhibit higher spin Hall efficiency compared to other heavy metals such as Pt. However, the larger resistivity of β-phase Ta leads to higher power consumption for spin−orbit torque (SOT)-based devices. In this work, we measure the efficiency of damping-like torque and field-like torque in $Ni_{80}Fe_{20}$/Ta using spin-torque ferromagnetic resonance technique. We report a larger damping-like torque efficiency of $-(0.52 \pm 0.01)$ for $Ni_{80}Fe_{20}$/Ta with low-resistive mixed $(\alpha + \beta)$-phase Ta, which is about 40% larger compared to β-phase Ta. The field-like torque efficiency is found to be lower (by ≈400%) and of opposite sign compared to β-phase Ta. The estimated power consumption is found to be lower in the mixed-phase Ta system compared to the β-phase Ta as well as some Pt-based systems. Using micromagnetic simulations, we show that the measured values of damping-like torque and field-like torque for mixed-phase Ta lead to improved device performance, namely, (i) a lower switching time in a nanopillar-based SOT device and (ii) improved phase noise in a nanoconstriction-based spin Hall nano-oscillator.

KEYWORDS: *spin−orbit torques, damping-like efficiency, spin Hall effect, Rashba effect, magnetization switching, spin Hall nano-oscillator*

■ INTRODUCTION

The spin of the electron, which is a quantum mechanical property, is utilized in the field of spintronics to realize energy-efficient electronic devices. A recent interest in the field of spintronics is the so-called spin−orbit torques (SOTs) typically observed in ferromagnetic/heavy metal (FM/HM) heterostructures .[1] The SOT allows use of current instead of magnetic field to manipulate orientation of magnetization[2−6] or even magnetic textures such as domain walls,[7,8] skyrmions,[9−11] and so forth. The application can be divided into two broad areas: (i) SOT-based magnetic random access memory and (ii) SOT-based spin Hall nano-oscillators (SHNOs)[4,6] for on-chip microwave wireless communication and neuromorphic computing.[12] In the first case of magnetic random access memory, the macroscopic magnetization or the motion of magnetic texture such as skyrmion occurs via SOT, while in the second case, the magnetization is driven into auto-oscillations when SOT counteracts the damping in the FM layer. These SOT-based spintronic devices offer high endurance, fast switching speed, and low power consumption compared to existing technology.[1,13−16]

The physical origin of SOT is attributed to two possible mechanisms, namely, (1) the spin Hall effect (SHE)[17−20] and (2) the Rashba effect[21−23] both of which can coexist. The SHE mechanism of SOT arises from a pure spin current created in the bulk of HM due to the spin−orbit coupling, while the Rashba mechanism of SOTs, also known as the inverse spin galvanic effect, arises from the breaking of inversion symmetry at the interface and the high spin−orbit coupling of the HM

Received: April 17, 2021
Accepted: June 28, 2021
Published: July 12, 2021

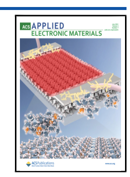

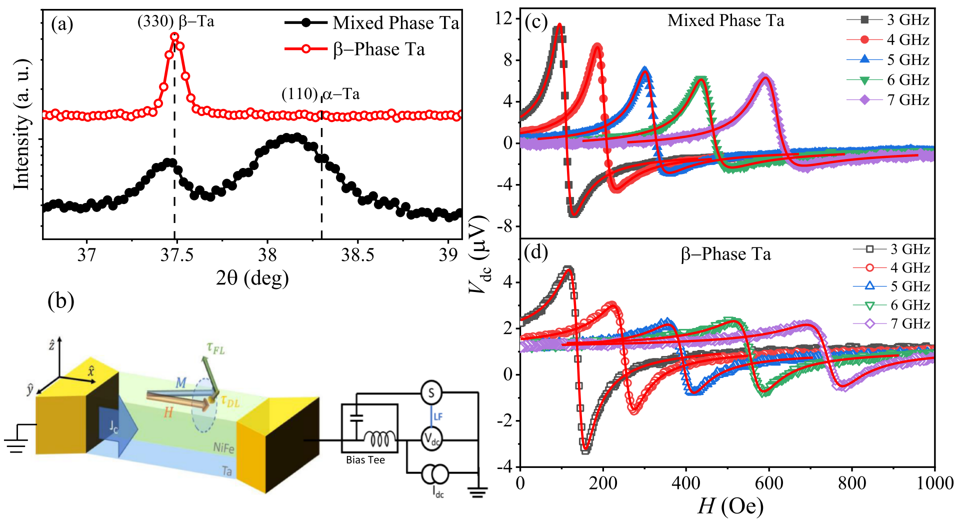

Figure 1. (a) XRD patterns for both Py/mixed-phase Ta and Py/β-phase Ta with dashed lines representing the expected Bragg positions for the bulk Ta. (b) Schematic of the bilayer microstrip with DLT (τ_{DL}) and FLT (τ_{FL}) generated by electrical current density J_C flowing along the x-axis. The external field is applied in the plane of the sample (XY plane). The schematic also illustrates the STFMR measurements setup, where a bias tee is used to feed and measure AC and DC signals. (c,d) Measured STFMR signal with the magnetic field applied at an angle of 45° with respect to the x-axis at various frequencies for (b) Py/mixed-phase Ta and (c) Py/β-phase Ta; the solid lines represent fits with eq 2.

layer. The charge-to-spin current efficiency due to the SHE is quantified using spin Hall angle (θ_{SH}) as

$$\theta_{SH} = \frac{2e}{\hbar}\frac{J_S}{J_C} \tag{1}$$

Here, e and $\hbar$ are the electronic charge and the reduced Planck's constant, respectively. J_S and J_C are the spin current density and the charge current density, respectively. The threshold energy in SOT devices varies inversely with θ_{SH},[24] and hence higher θ_{SH} is desirable for applications. Another important parameter for applications is the resistivity of heavy metals, which should be lower for minimizing power consumption in SOT devices. The β-phase of Ta thin films has been known to manifest larger θ_{SH} compared to the commonly used heavy metal Pt.[24,25] However, the β-phase of Ta is also a high-resistive phase and hence consumes more power in a SOT-based device. Thus, the low-resistive phase of Ta, which also exhibits higher spin Hall angle,[26] is desirable for SOT-based devices. Both SHE and Rashba mechanism can generate a damping-like torque (DLT, τ_{DL}) and a field-like torque (FLT, τ_{FL}),[1,3,27−30] though the SHE mechanism is often assumed to have a larger contribution to DLT. For a spin current with spin polarization along $\hat{y}$, the DLT has the form $\tau_{DL} \propto \vec{M} \times (\hat{y} \times \vec{M})$, while the FLT has the form $\tau_{FL} \propto \hat{y} \times \vec{M}$, where $\vec{M}$ represents the magnetization of the FM layer. Due to different symmetries of DLT and FLT, they affect magnetization dynamics very differently. Some of the initial studies did not consider the presence of FLT in the FM/HM bilayer system.[2,24] However, recent studies show the presence of sizable FLT in several FM/HM systems.[31,32] While the DLT is known to reduce threshold switching current, the effect of FLT and its sign is not studied in detail.

In this work, we measure the strength of DLT and FLT efficiencies in the $Ni_{81}Fe_{19}$ (or Py)/Ta system using the bias dependence of spin-torque ferromagnetic resonance (STFMR)[2,33,34] for two different crystalline phases of the Ta layer. We found a larger DLT efficiency of $-(0.52 \pm 0.01)$ for Py/Ta with low-resistive mixed ($\alpha + \beta$)-phase Ta, which is about 40% larger compared to high-resistive β-phase Ta. The FLT efficiency is found to be lower (by ≈400%) and of the opposite sign compared to β-phase Ta. The estimated power consumption for the Py/mixed-phase Ta system exceeds that of the Pt-based heterostructures. To study the effect of the measured DLT and FLT efficiencies on FM/HM system-based device applications, we performed micromagnetic simulations on switching time and auto-oscillation properties. We observe a lower switching time for mixed-phase Ta in a nanopillar device. Furthermore, the phase noise is significantly reduced in mixed-phase Ta-based nano-constriction SHNOs.

■ MATERIALS AND EXPERIMENTAL METHODS

The bilayer films of Py(4 nm)/Ta(13 nm) are deposited on sapphire (Al_2O_3) substrates using DC magnetron sputtering at room temperature. The growth rate of Ta thin films are optimized for pure β-phase and mixed ($\alpha + \beta$) phase of Ta thin films by varying the sputtering power. Details can be found in our earlier work on Si substrates.[26,35] The samples discussed in this work consist of two kinds of Ta layers of the same thickness (13 nm) but different growth rates of 1.88 and 0.62 Å/s. The thickness and interface roughness of the layers were found using X-ray reflectivity measurements.[36]

Figure 1a shows the XRD measurements (θ−2θ scan) for samples grown at a growth rate of 1.88 and 0.62 Å/s corresponding to pure β-phase (open symbols) and mixed-phase (solid symbols) Ta, respectively. We observed Bragg peak at 37.4° corresponding to the (330) diffraction peak of tetragonal β-phase Ta instead of (002) diffraction which was observed in our previous work on the Si substrate.[26,35,37] The Bragg peak at 38.2° corresponding to the (110) diffraction peak of body-centered α-phase Ta is observed only for the sample with a growth rate of 0.62 Å/s. This indicates that the sample with a growth rate of 0.62 Å/s exhibits a mixed crystalline phase. However, the position of the (330) peak of tetragonal β-phase Ta as well as that of the (110) peak in α-phase Ta is slightly shifted with respect to the expected bulk positions shown by dashed lines, indicating a slightly different lattice parameter. In fact, this variation of lattice constant with growth rate as well as the sputtering working pressure in the Ta thin film is known in the literature.[38] The β-phase sample is found to be polycrystalline [as observed by the long-range X-ray diffraction (XRD) measurements, see the Supporting Information.[36]] These structural results are different from our previous studies, where the thin films grown on the Si/SiO_2 substrate exhibited oriented β-phase Ta. The resistivity of Py and Ta thin films was measured using four-point resistance measurements. First, the resistivity of single-layer Py was measured and found to be 46 $\mu\Omega$ cm. For mixed-phase and β-phase Ta, the values are found to be 89 and 200 $\mu\Omega$ cm, respectively.

For STFMR measurements, the DC and radio frequency (RF) current was passed along the long axis of the bar (x-axis) using a bias tee, while the field was applied in the XY-plane (schematic is shown in Figure 1b) at an in-plane angle $\phi = 45°$ with respect to the current. We use a RF modulation-based STFMR setup for improved signal-to-noise ratio. The RF current generated by the signal generator was amplitude-modulated (low frequency), and the rectified voltage was detected using a lock-in amplifier.[34]

RESULTS AND DISCUSSION

Zero-Bias STFMR Measurements. The typical STFMR spectra for various radio frequencies (f) at zero DC bias are shown in Figure 1c,d for Py/mixed (solid symbols) and Py/β-phase (open symbols) Ta, respectively. A fixed RF power of +5 dBm is used for all our measurements. Here, the solid lines are the fitting of the observed signal with the following form[2,34]

$$V_{dc} = V_S \frac{\Delta H^2}{\Delta H^2 + (H - H_R)^2} + V_A \frac{\Delta H (H - H_R)}{\Delta H^2 + (H - H_R)^2} \quad (2)$$

Here, V_S and V_A are symmetric and antisymmetric Lorentzian peak voltages. Moreover, H, ΔH, and H_R represent the external magnetic field, linewidth, and resonance field, respectively.

Following the standard model of STFMR, the spin Hall angle θ_{SH} can be quantitatively determined using the ratio V_S/V_A[2,34]

$$\theta_{SH} = \frac{V_S}{V_A} \frac{e\mu_0 M_S t_{FM} d_{NM}}{\hbar} \left[1 + \frac{4\pi M_{eff}}{H_R}\right]^{1/2} \quad (3)$$

Here, d_{NM} and t_{FM} are the nonmagnetic and FM layer thicknesses, respectively. e, $\hbar$, and M_S represent the electric charge, reduced Planck's constant, and saturation magnetization, respectively. We calculate the effective magnetization M_{eff} from the fitting of f *versus* H_R (obtained from eq 2) data using Kittel formula.[36] We found $M_{eff} = 705 \pm 3$ Oe for mixed-phase Ta/Py and $M_{eff} = 717 \pm 4$ Oe for β-phase Ta/Py. From the ratio of V_S/V_A, we obtain $\theta_{SH} = -(0.220 \pm 0.004)$ for Py/mixed-phase Ta and $\theta_{SH} = -(0.08 \pm 0.01)$ for the Py/β-phase Ta sample by averaging over the measured frequency range of 4−7 GHz.

However, in the above analysis, the voltage contributions due to spin pumping-induced inverse SHE are neglected, considering this contribution will lead to further enhancement of θ_{SH}.[39] Furthermore, the above eq 3 assumes that the V_A is only determined by the Oersted field due to the RF magnetic field, and it neglects the presence of FLT. As reported by Allen et al.,[31] FLT is known to be finite and significant in β-phase Ta systems. In fact, the FLT can arise due to both the Rashba effect and SHE[40] and is present in almost every FM/HM interface. Due to these issues, the zero bias method is somewhat inaccurate in determining the correct damping-like efficiency.[40] Hence, we use DC bias (I_{DC})-dependent STFMR measurements to extract the damping-like efficiency, which in addition also allow for the determination of FLT efficiencies.

Bias-Dependent STFMR Measurements. We used effective Gilbert damping (α) *versus* I_{DC} to extract DLT and the resonance field (H_R) *versus* I_{DC} to extract the FLT efficiencies, discussed in the following text. Figure 2a,b shows

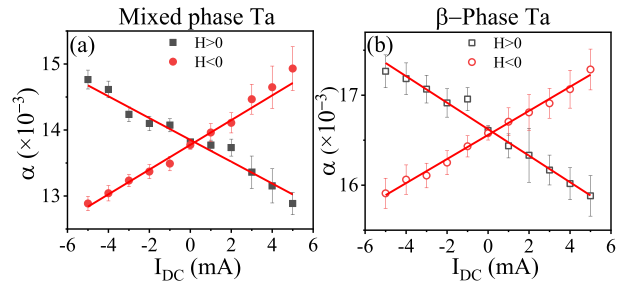

Figure 2. (a,b) Variation of Gilbert damping constant (α) with the total applied DC bias (I_{DC}) at positive (45°) and negative applied fields (225°) for Py/mixed-Ta and Py/β-Ta, respectively. The lines represent linear fit of the data.

the behavior of α as a function of I_{DC} for Py/mixed- and Py/β-phase Ta, respectively. The damping constant is determined from the frequency variation of linewidth at each current. For a positive field, the slope of damping constant *versus* DC bias is negative, whereas for a negative field, the slope become positive as expected from the symmetry of spin−orbit torque. For a total injected current of $I_{DC} = \pm 5$ mA, we achieve 11.1% modulation of the Gilbert damping in Py/mixed-phase Ta bilayer thin films (Figure 2a), where % modulation of Gilbert damping is defined as $[\alpha(I_{DC} = 0) - \alpha(I_{DC} \neq 0)/\alpha(I_{DC} = 0)] \times 100\%$. However, for Py/$\beta$-phase Ta (Figure 2b), % modulation of Gilbert damping is only 4.2%. This is an indication of lower DLT efficiency in Py/β-phase Ta. We quantify the DLT efficiency (ξ_{DL}) from the current-induced modulation of damping data by using the following equation[2,41]

$$\xi_{DL} = \frac{2e}{\hbar} \frac{M_S w t_{FM}{}^2}{\sin\phi} [\mu_0 H_R + 0.5\mu_0 M_S] \times \frac{\Delta\alpha}{\Delta I_{DC}^{Ta}} \quad (4)$$

$\Delta\alpha/\Delta I_{DC}^{Ta}$ is calculated from Figure 2a,b for Py/mixed- and Py/β-phase Ta, respectively. Here, w is the width of the STFMR devices. The current in the Ta layer, I_{DC}^{Ta}, is calculated from the total current I_{DC} using a parallel resistor model from the measured resistivity of individual layers. The DLT efficiency ξ_{DL} is found to be $-(0.52 \pm 0.01)$ and $-(0.37 \pm 0.02)$ for Py/mixed- and Py/β-phase Ta, respectively. Since we determine these efficiencies from Gilbert damping (which is determined from the slope of ΔH *vs* f[36]), the values also represent frequency average values. Thus, the DLT efficiency ξ_{DL} is found to be about 40% larger for mixed-phase Ta as compared to β-phase Ta. The larger DLT efficiency of Py/mixed-phase Ta is promising for various SOT applications. Since mixed-phase Ta is a low-resistive phase, the power consumption in a SOT device will be lower, which will be discussed in detail in Power Consumption.

The STFMR measurements with finite I_{DC} also allow for an accurate estimation of FLT efficiency.[32,42] We use H_R *versus* I_{DC} behavior to determine the FLT efficiency, as shown in Figure 3a,b for Py/mixed- and β-phase Ta, respectively. We use the method proposed by Kim et al.,[32] which uses a linear change in the resonance field of the STFMR spectra to extract the FLT efficiency. To remove the thermal artifacts and Oersted field from the H_R *versus* I_{DC} data, the even and odd components of H_R are extracted using $[H_R(I_{DC}) - H_R(0)] \pm [H_R(-I_{DC}) - H_R(0)]/2$, where a (+) or (−) sign describes an even or odd component. Figure 3c−f shows the shift of the even and odd components of H_R with I_{DC} for Py/mixed- and

https://doi.org/10.1021/acsaelm.1c00361
ACS Appl. Electron. Mater. 2021, 3, 3139−3146

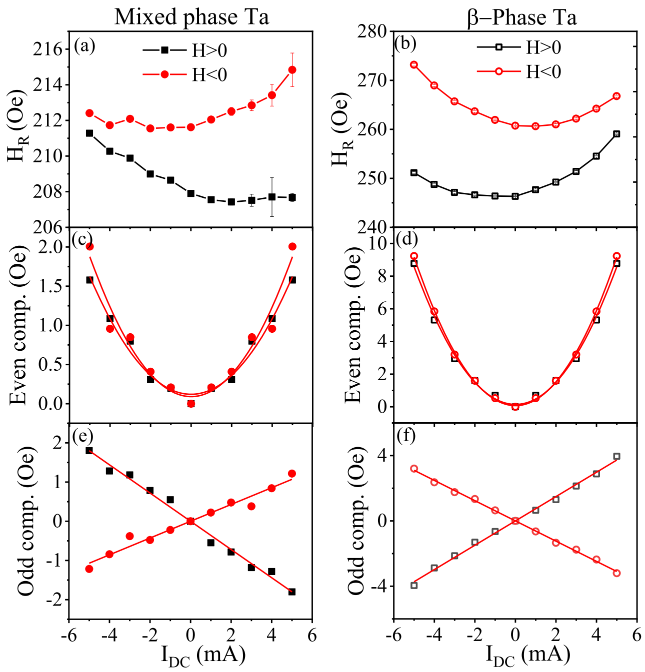

Figure 3. Modulation of resonance field (H_R) (a,b) and extracted even component (c,d) and odd component (e,f) with applied DC bias current for Py/mixed-phase Ta (first column) and Py/β-phase Ta (second column). The solid lines in (c,d) are parabolic fits, while those in (e,f) are linear fits.

Py/β-phase Ta, respectively. The FLT efficiency is then calculated using the change in the odd component of the *HR*[32] after subtracting the Oe field

$$\xi_{FL} = \frac{2e}{\hbar}\left(\frac{\Delta H_R}{\Delta I_{DC}^{Ta}} \times \frac{1}{\sin\phi}\frac{R_{Py} + R_{Ta}}{R_{Py}}A_{C,NM}C - \frac{d_{NM}}{2}\right) \times \mu_0 M_S t_{FM} \quad (5)$$

Here, R_{Py} and R_{Ta} are the resistances of the Py and Ta layers, respectively. Here, C is 1 for the FM/HM combination and −1 for HM/FM. $A_{C,NM}$ is the area of the cross section of the nonmagnetic Ta layer. $\Delta H_R/\Delta I_{DC}^{Ta}$ represents the slope of the odd component of H_R *versus* I_{DC} as shown in Figure 3e,f for Py/mixed- and Py/β-phase Ta, respectively. The even component behaves quadratically with the bias current (solid line), indicating that it is caused by Joule heating. In the odd component, $\Delta H_R/\Delta I_{DC}^{Ta}$ is found to be similar for the positive ($+H$) and negative ($-H$) magnetic fields. We have taken the average value of $+H$ and $-H$ for the $\Delta H_R/\Delta I_{DC}$ calculations in eq 5. Using this method, the FLT efficiency is found to be −(0.06 ± 0.01) for mixed-phase Ta and (0.17 ± 0.01) for β-phase Ta. The FLT efficiency of the mixed phase is thus found to be lower by ≈400% and of opposite sign compared to β-phase Ta. The sign change implies that the FLT in Py/β-phase Ta is oppositely oriented with respect to the Oersted field compared to Py/mixed-phase Ta.

Table 1 shows the summary of all parameters of Py/mixed-phase and Py/β-phase Ta samples. The results were reproduced in several other devices of both Py/mixed and Py/β-phase Ta. The damping-like efficiencies measured using the symmetric component (θ_{SH}) as well as modulation of damping (ξ_{DL}) are both found to be significantly higher (40%) for Py/mixed-phase Ta compared to Py/β-phase Ta. On the other hand, the strength of ξ_{FL} is found to be higher and of opposite sign for Py/β-phase Ta as opposed to Py/mixed-phase Ta. The change in ξ_{FL} is approx. 400% (considering the sign) for Py/β-phase Ta with respect to Py/mixed-phase Ta.

Table 1. Summary of Measured Parameters: θ_{SH} and % Current Modulation of Damping, ξ_{DL} and ξ_{FL}

Ta phase	θ_{SH}	ξ_{DL}	ξ_{FL}
$\alpha + \beta$	−0.220 ± 0.004	−0.52 ± 0.01	−0.06 ± 0.01
B	−0.08 ± 0.01	−0.37 ± 0.02	0.17 ± 0.01

These values of SOT efficiencies represent a lower limit as we have not considered spin memory loss[43] and spin back flow. The intrinsic spin Hall efficiency is generally larger than these measured values. However, in our samples, the thickness of the nonmagnetic layer (Ta) is larger than the maximum reported values of spin diffusion length (λ_{SD} = 5.1 nm).[44] Hence, the spin back flow is negligible in our samples. Similarly, we also believe that the spin memory loss is negligible in our samples due to the following reasons. The recent experimental results by Panda et al[45] and Chang et al.[46] have shown significantly lower spin memory loss in the Ta/FM system compared to the Pt-based system. Chang et al.[46] have also shown that inserting a Cu spacer between Co/Ta even reduces the SOT, further confirming lower spin memory loss in the Co/Ta interface compared to Co/Cu. Furthermore, according to recent studies by Zhu et al.,[47] spin memory loss scales linearly with interfacial spin−orbit coupling. Zhu et al. used the interfacial magnetic anisotropy energy density K_s as a measure of interfacial spin−orbit coupling. In our system, we found K_s = 0.39 ergs/cm^2 for the Py/mixed-phase Ta interface and K_s = 0.37 ergs/cm^2 for the β-phase Py/Ta interface. Both these values are comparable and significantly lower than the value for the Pt-based system used by Zhu et al., where K_s was found to vary between 1 and 3.5 ergs/cm^2. In fact, our value of K_s is even lower than that of the Co/MgO interface of Zhu et al. This low value of K_s indicates negligible interfacial spin−orbit coupling and spin memory loss in our system.

Both the Rashba mechanism and SHE mechanism in an FM/HM bilayer can produce damping-like SOT as well as field-like SOT. However, it is often assumed that SHE generates a dominating DLT, while Rashba mechanism generates a dominating FLT.[1,3,27−30] Based on this, we speculate that the larger DLT in mixed-phase Ta is due to a dominating SHE mechanism of SOT in Py/mixed-phase Ta, while the larger ξ_{FL} in the case of Py/β-phase Ta (which is also accompanied by a sign change of ξ_{FL}) is due to a dominating Rashba mechanism in Py/β-phase Ta. In fact, recently, a sign change of ξ_{FL} was found in Cr/Ni heterostructures[48] due to the Rashba mechanism. For mixed-phase Ta, the spin Hall conductivity is found to be −2471 $\hbar$/e Ω^{-1} cm^{-1}. The first-principles calculation showed that the intrinsic spin Hall conductivity of β-Ta is −378 $\hbar$/e Ω^{-1} cm^{-1}, while that of α-Ta is −100 $\hbar$/e Ω^{-1} cm^{-1},[49] both of which are significantly lower than our observation. Hence, we believe that the larger damping-like SOT in mixed-phase Ta is caused by extrinsic SHE due to a disordered crystalline structure.

Power Consumption. In order to show the benefit of low-resistive mixed-phase Ta for SOT-based device applications, we calculate the power consumption in this section. Power consumption (P_{loss}) by SOT devices with FM/HM bilayer structures can be determined by calculating power loss by individual layers.[50,51]

$$P_{\text{loss}} = I_{\text{DC}}^{2} \frac{\rho_{\text{Py}}\rho_{\text{Ta}}}{(\rho_{\text{Py}} + \rho_{\text{Ta}})^2} \left[\frac{\rho_{\text{Ta}}}{t_{\text{FM}}} + \frac{\rho_{\text{Py}}}{d_{\text{Ta}}} \right] \frac{L}{w} \tag{6}$$

Here, ρ_{Py} and ρ_{Ta} are Py and Ta resistivities and L and w are the length and width of the microstrip structure. We have calculated power consumption in the case of mixed- and β-phase Ta thin films and found it to be 3.63 mW at I_{DC} = 5 mA, which is lower than that reported for Pt.[2] However, β-phase shows larger P_{loss} (6.11 mW) compared to both mixed-phase Ta and reported values for Pt. Power consumption in our bilayer system is 7 times smaller than the reported value of β-Ta by Liu et al..[24] However, Liu et al. used CoFeB as a ferromagnet, which has larger resistivity. This increases the total power consumption in their case. We have also compared our results with high-resistive β-phase W thin films.[51] A detailed comparison of θ_{SH} and power consumption with other reports (for which data for 5 mA was available) is shown in Table 2. The table shows that the power consumption is lower in our case of mixed-phase Ta. Using the pioneering work of Liu et al.[24] as a reference, the power consumption in our case is about 12% lower, with θ_{SH} nearly 4 times. If we consider DLT efficiency determined from the current modulation of linewidth, then ξ_{DL} is nearly an order of magnitude higher than Pt in the study by Liu et al.[24]

Table 2. Comparison of Spin Hall Efficiency (θ_{SH}), Power Consumption, and Normalized Power Consumption for SOT Applications at 5 mA

sample	θ_{SH}	P_{loss} (mW) at 5 mA	normalized power consumption	ref
Py/Ta (mixed-phase)	−0.22	3.16 ± 0.09	0.88	this work
Py/Ta (β-phase)	−0.08	6.1 ± 0.2	1.69	this work
Py/Pt	0.06	3.6	1.00	2
CoFeB/β-Ta	−0.12	21.8	6.05	24
CoFeB/β-W	−0.30	7.4	2.05	51

Impact of Measured SOT Efficiencies on Device Performance. We observe a large DLT in Py/mixed-phase Ta and an opposite sign and a larger FLT in Py/β-phase Ta. In order to understand the impact of these parameters on the device applications using SOT, we performed micromagnetic simulations for two possible devices, namely, SOT-magnetic random-access memories and SOT-based SHNOs for microwave communication and neuromorphic computing applications.[6,52,53] In the absence of FLT, the stronger DLT reduces the critical current for magnetization switching[54] and auto-oscillations[6,53] of magnetization in the SOT-based devices. However, in the presence of both DLT and FLT, the behavior is expected to be complex. In particular, the impact of sign change of FLT together with the change in DLT is investigated in this section. We performed micromagnetic simulations using Mumax3[55] for two geometries: (i) an elliptical nanopillar to observe magnetization switching for SOT-magnetic random access memory applications (shown in Figure 4a) and (ii) a nanoconstriction-based SHNO (shown in Figure 4b). We utilized the experimental parameters extracted from our STFMR measurements given in Table 1. In addition, we used a small in-plane magnetic anisotropy ($K = 0.5 \times 10^3$ J/m^3) along the y-direction and an exchange stiffness constant (A_{ex} = 10 pJ/m) of Py.[56,57] The Mumax^3 module incorporates the spin-transfer torques (τ_{SL}) in the Slonczewski form, transformed to the Landau−Lifshitz formalism[55] as:

$$\vec{\tau}_{\text{SL}} = -\beta \frac{\varepsilon - \alpha\varepsilon'}{1+\alpha^2} (\hat{m} \times (\hat{m} \times \hat{p})) - \beta \frac{\varepsilon' - \alpha\varepsilon}{1+\alpha^2} (\hat{m} \times \hat{p}) \tag{7}$$

where ϵ and ϵ' are the spin-torque parameters and $\beta = J_s/M_s e t_{\text{FM}}$. We consider $\epsilon = P/2$, where P is the spin polarization.

For a very small value of α (<0.05), we can incorporate the damping-like efficiency as $\xi_{\text{DL}} = P/2$ and field-like efficiency as $\xi_{\text{FL}} = \epsilon'$ in the Mumax^3 module for SOT-based simulations. $\hat{p}$ denotes the direction of spin polarization, which is taken to be along $\hat{y}$ for a charge current along the x-axis as per the symmetry of the SOT.

Effect on Switching Current. For the SOT switching, we consider an elliptical nanopillar geometry of dimension (60 nm × 100 nm × 4 nm), which is discretized into a small cell of size 1 nm × 1 nm × 4 nm. As shown in Figure 4a, the charge current ($J_{\vec{c}}$) is assumed to be along the +ve x-axis which produces a spin current ($J_{\vec{s}}$) in the out-of-plane direction with a polarization ($\vec{p}$) along the y-axis. The initial magnetization ($\vec{m}$) of Py is assumed to be along the +ve y-axis. Figure 4c shows the SOT-induced switching of the y-component of magnetization for two different cases (β- and mixed-phase Ta) at a fixed current density, $J_s = 9 \times 10^{12}$ A/m^2. The switching time is found to be t_β = 63 ps for the case of β phase and t_{Mixed} = 35 ps for the mixed phase. Hence, the switching (t_β) time for β-phase Ta is 1.8 times higher compared to the switching (t_{mixed}) time for mixed-phase Ta. In addition, we also see an incubation delay in the SOT switching data for β-phase Ta, which was recently reported in real-time experimental data on SOT-induced switching in magnetic tunnel junctions.[58]

Effect on Auto-Oscillations and Phase Noise. In order to investigate the influence on the auto-oscillations for microwave communication applications, we have chosen a nanoconstriction-based SHNO geometry with a 150 nm width of nanoconstriction in a thin film of Py of dimension 2 μm × 2 μm × 5 nm. The cell size for simulation is 3.9 nm × 3.9 nm × 5 nm. To achieve sustained auto-oscillation in the SHNO, we have used an external in-plane magnetic field (40 mT) at an angle 60° with respect to the x-axis.[12,59] The auto-oscillation was confirmed by performing simulations over a long time around 2000 ns. The fast Fourier transform (FFT) in Figure 4e inset shows a clear auto-oscillation frequency of 5.05 GHz (period of 0.2 ns), where the amplitude and linewidth of auto-oscillation are comparatively better in mixed-phase Ta as compared to β-phase Ta. The simulation time (2000 ns) is about 10,000 times the period of oscillations (0.2 ns). Since we use parameters measured at room temperature, a temperature of 300 K in micromagnetic simulations will overestimate the effect of temperature. Hence, we used 50 K in our simulation to include finite temperature effects. To determine the threshold current for auto-oscillations, we perform simulation as a function of DC bias with a Gaussian profile at the center of nano-constriction of SHNO. The threshold current is determined by using the inverse of outpower *versus* bias current as shown in Figure 4d.[60] It is evident that the β-phase Ta system requires a slightly larger threshold current, which can be understood as a result of lower DLT efficiency. In order to show the impact of measured FLT efficiency on the performance of SHNOs, we determine phase noise, which is important for applications. The phase noise is calculated from the simulated time-domain data using the zero crossover

https://doi.org/10.1021/acsaelm.1c00361
ACS Appl. Electron. Mater. 2021, 3, 3139−3146

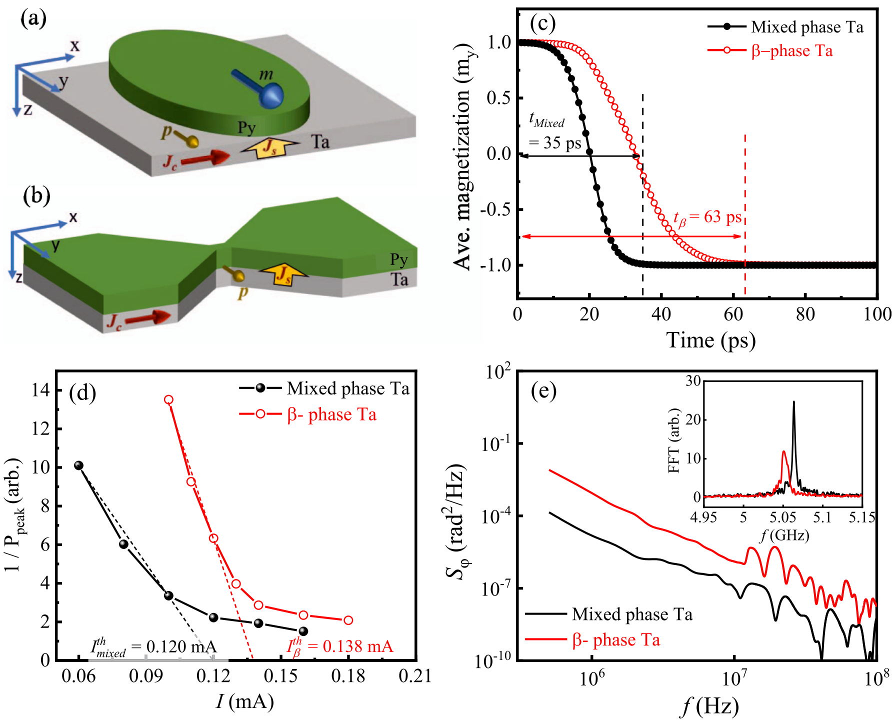

Figure 4. (a,b) Schematic of the elliptical nanopillar and nanoconstriction SHNO for studying the magnetic switching and auto-oscillations in Py/Ta bilayers, respectively. (c) Comparison of the switching time in an elliptical nanopillar geometry for β- and mixed-phase Ta at a fixed current density $J_s = 9 \times 10^{12}$ A/m^2. (d) Dependence of $1/P_{peak}$ (inverse of peak to peak value of output power of SHNO) as a function of injected current (I). The extrapolated dotted lines (red and black) correspond to the threshold current for auto-oscillation (mixed- and β-phase), respectively. (e) Simulated phase noise for SOT-based nanoconstriction SHNO using mixed-phase (black) and β-phase Ta (red) system at current values equal to the corresponding threshold currents as determined in (d), where the inset shows the FFT plot for auto-oscillation corresponding to mixed-phase Ta (black) and β-phase Ta (red).

method.[61] Figure 4e shows the simulated phase noise (S_ϕ) for mixed-phase (black line) and β-phase Ta (red line) at the threshold condition. Both the plots show the typical $1/f^2$ phase noise behavior.[62,63] It is found that the β-phase Ta system shows a much higher phase noise compared to mixed-phase Ta. This also leads to higher linewidth for the β-phase Ta system as shown in the inset of Figure 4e. We systematically studied the impact of FLT sign change on the phase noise and observed that the same sign of DLT and FLT (as in the mixed-phase Ta) efficiency reduces the phase noise and hence the linewidth. The same sign of DLT and FLT efficiency also assists the oscillation by increasing the oscillation amplitude. On the other hand, the opposite sign of FLT and DLT (as in β-phase Ta) efficiency increases the phase noise and linewidth and decreases the oscillation amplitude, adversely affecting the auto-oscillation performance. Hence, the same sign of FLT and DLT together with larger DLT in a mixed-phase Ta system is highly beneficial for SHNO device performance.

CONCLUSIONS

In summary, we find a 40% larger DLT for Py/Ta with mixed-phase Ta compared to β-phase Ta. We see a 400% lower FLT efficiency for Py/mixed-phase Ta with opposite sign compared to Py/β-phase Ta. We show that due to lower resistivity, the mixed phase of Ta leads to lower power consumption. The estimated power consumption for the Py/mixed-phase Ta system is found to be lower than the Pt-based heterostructures. We also show that the above properties lead to improved device performance for the Py/mixed-phase Ta system, namely, (i) a lower SOT switching time in a nanopillar device and (ii) a lower phase noise in a nanoconstriction-based SHNO.

METHODS

Device Fabrication and Measurements. For STFMR measurements, the bilayer thin films are fabricated in the form of arrays of rectangular mesas of 4 × 12 μm^2 using e-beam lithography (Raith e-line) followed by Ar ion-milling. After fabrication of rectangular mesas, ground-signal-ground coplanar wave guides are defined in a subsequent step, and Ta/Cu is deposited over them using a lift-off process. The STFMR measurements are performed using a signal generator (Rohde and Schwarz SMB 100A) and a lock-in amplifier (Stanford Research Systems SR830 DSP) coupled using a bias-tee.

ASSOCIATED CONTENT

Supporting Information

The Supporting Information is available free of charge at https://pubs.acs.org/doi/10.1021/acsaelm.1c00361.

X-ray reflectivity measurements of Al_2O_3/Py/Ta for both mixed-phase and β-phase Ta thin films; long-range XRD measurements; frequency-dependent STFMR measurements; and calculated spin Hall angle (PDF)

AUTHOR INFORMATION

Corresponding Author

Pranaba Kishor Muduli – *Thin Film Laboratory, Department of Physics, Indian Institute of Technology Delhi, Hauz Khas 110016 New Delhi, India;* orcid.org/0000-0002-0061-8455; Email: muduli@physics.iitd.ac.in

https://doi.org/10.1021/acsaelm.1c00361
ACS Appl. Electron. Mater. 2021, 3, 3139−3146

Authors

Akash Kumar − *Thin Film Laboratory, Department of Physics, Indian Institute of Technology Delhi, Hauz Khas 110016 New Delhi, India;* orcid.org/0000-0002-4105-3681

Raghav Sharma − *Thin Film Laboratory, Department of Physics, Indian Institute of Technology Delhi, Hauz Khas 110016 New Delhi, India*

Kacho Imtiyaz Ali Khan − *Thin Film Laboratory, Department of Physics, Indian Institute of Technology Delhi, Hauz Khas 110016 New Delhi, India*

Chandrasekhar Murapaka − *School of Physical and Mathematical Sciences, Nanyang Technological University, Singapore 637371, Singapore*

Gerard Joseph Lim − *School of Physical and Mathematical Sciences, Nanyang Technological University, Singapore 637371, Singapore*

Wen Siang Lew − *School of Physical and Mathematical Sciences, Nanyang Technological University, Singapore 637371, Singapore;* orcid.org/0000-0002-5161-741X

Sujeet Chaudhary − *Thin Film Laboratory, Department of Physics, Indian Institute of Technology Delhi, Hauz Khas 110016 New Delhi, India;* orcid.org/0000-0002-0535-6132

Complete contact information is available at: https://pubs.acs.org/10.1021/acsaelm.1c00361

Notes

The authors declare no competing financial interest.

■ ACKNOWLEDGMENTS

The partial support from the Ministry of Human Resource Development under the IMPRINT program (grant nos 7519 and 7058), the Department of Electronics and Information Technology (DeitY), and the Department of Science and Technology under the Nanomission program (grant no SR/NM/NT—1041/2016(G)) is gratefully acknowledged. A.K. acknowledges support from the Council of Scientific and Industrial Research (CSIR), India.

■ REFERENCES

(1) Manchon, A.; Železný, J.; Miron, I. M.; Jungwirth, T.; Sinova, J.; Thiaville, A.; Garello, K.; Gambardella, P. Current-induced spin-orbit torques in ferromagnetic and antiferromagnetic systems. *Rev. Mod. Phys.* **2019**, *91*, 035004.

(2) Liu, L.; Moriyama, T.; Ralph, D. C.; Buhrman, R. A. Spin-Torque Ferromagnetic Resonance Induced by the Spin Hall Effect. *Phys. Rev. Lett.* **2011**, *106*, 036601.

(3) Miron, I. M.; Garello, K.; Gaudin, G.; Zermatten, P.-J.; Costache, M. V.; Auffret, S.; Bandiera, S.; Rodmacq, B.; Schuhl, A.; Gambardella, P. Perpendicular switching of a single ferromagnetic layer induced by in-plane current injection. *Nature* **2011**, *476*, 189−193.

(4) Demidov, V. E.; Urazhdin, S.; Ulrichs, H.; Tiberkevich, V.; Slavin, A.; Baither, D.; Schmitz, G.; Demokritov, S. O. Magnetic nano-oscillator driven by pure spin current. *Nat. Mater.* **2012**, *11*, 1028.

(5) Ando, K.; Saitoh, E. Observation of the inverse spin Hall effect in silicon. *Nat. Commun.* **2012**, *3*, 629.

(6) Chen, T.; Dumas, R. K.; Eklund, A.; Muduli, P. K.; Houshang, A.; Awad, A. A.; Durrenfeld, P.; Malm, B. G.; Rusu, A.; Åkerman, J. Spin-Torque and Spin-Hall Nano-Oscillators. *Proc. IEEE* **2016**, *104*, 1919−1945.

(7) Haazen, P. P. J.; Murè, E.; Franken, J. H.; Lavrijsen, R.; Swagten, H. J. M.; Koopmans, B. Domain wall depinning governed by the spin Hall effect. *Nat. Mater.* **2013**, *12*, 299−303.

(8) Hrabec, A.; Sampaio, J.; Belmeguenai, M.; Gross, I.; Weil, R.; Chérif, S. M.; Stashkevich, A.; Jacques, V.; Thiaville, A.; Rohart, S. Current-induced skyrmion generation and dynamics in symmetric bilayers. *Nat. Commun.* **2017**, *8*, 15765.

(9) Montoya, S. A.; Tolley, R.; Gilbert, I.; Je, S.-G.; Im, M.-Y.; Fullerton, E. E. Spin-orbit torque induced dipole skyrmion motion at room temperature. *Phys. Rev. B* **2018**, *98*, 104432.

(10) Avci, C. O.; Rosenberg, E.; Caretta, L.; Büttner, F.; Mann, M.; Marcus, C.; Bono, D.; Ross, C. A.; Beach, G. S. D. Interface-driven chiral magnetism and current-driven domain walls in insulating magnetic garnets. *Nat. Nanotechnol.* **2019**, *14*, 561−566.

(11) Sisodia, N.; Komineas, S.; Muduli, P. K. Chiral skyrmion auto-oscillations in a ferromagnet under spin-transfer torque. *Phys. Rev. B* **2019**, *99*, 184441.

(12) Zahedinejad, M.; Awad, A. A.; Muralidhar, S.; Khymyn, R.; Fulara, H.; Mazraati, H.; Dvornik, M.; Åkerman, J. Two-dimensional mutually synchronized spin Hall nano-oscillator arrays for neuromorphic computing. *Nat. Nanotechnol.* **2020**, *15*, 47−52.

(13) Ikeda, S.; Miura, K.; Yamamoto, H.; Mizunuma, K.; Gan, H. D.; Endo, M.; Kanai, S.; Hayakawa, J.; Matsukura, F.; Ohno, H. A perpendicular-anisotropy CoFeB-MgO magnetic tunnel junction. *Nat. Mater.* **2010**, *9*, 721.

(14) Sato, H.; Yamanouchi, M.; Ikeda, S.; Fukami, S.; Matsukura, F.; Ohno, H. MgO/CoFeB/Ta/CoFeB/MgO recording structure in magnetic tunnel junctions with perpendicular easy axis. *IEEE Trans. Magn.* **2013**, *49*, 4437−4440.

(15) Yuasa, S.; Hono, K.; Hu, G.; Worledge, D. C. Materials for spin-transfer-torque magnetoresistive random-access memory. *MRS Bull.* **2018**, *43*, 352−357.

(16) Sato, N.; Xue, F.; White, R. M.; Bi, C.; Wang, S. X. Two-terminal spin-orbit torque magnetoresistive random access memory. *Nat. Electron.* **2018**, *1*, 508−511.

(17) Dyakonov, M. I.; Perel, V. I. Current-induced spin orientation of electrons in semiconductors. *Phys. Lett. A* **1971**, *35*, 459−460.

(18) Hirsch, J. E. Spin Hall Effect. *Phys. Rev. Lett.* **1999**, *83*, 1834−1837.

(19) Hoffmann, A. Spin Hall effects in metals. *IEEE Trans. Magn.* **2013**, *49*, 5172−5193.

(20) Sinova, J.; Valenzuela, S. O.; Wunderlich, J.; Back, C. H.; Jungwirth, T. Spin Hall effects. *Rev. Mod. Phys.* **2015**, *87*, 1213−1260.

(21) Bychkov, Y. A.; Rashba, É. I. Properties of a 2D electron gas with lifted spectral degeneracy. *JETP Lett.* **1984**, *39*, 78.

(22) Edelstein, V. M. Spin polarization of conduction electrons induced by electric current in two-dimensional asymmetric electron systems. *Solid State Commun.* **1990**, *73*, 233−235.

(23) Bihlmayer, G.; Rader, O.; Winkler, R. Focus on the Rashba effect. *New J. Phys.* **2015**, *17*, 050202.

(24) Liu, L.; Pai, C.-F.; Li, Y.; Tseng, H. W.; Ralph, D. C.; Buhrman, R. A. Spin-Torque Switching with the Giant Spin Hall Effect of Tantalum. *Science* **2012**, *336*, 555.

(25) Sagasta, E.; Omori, Y.; Vélez, S.; Llopis, R.; Tollan, C.; Chuvilin, A.; Hueso, L. E.; Gradhand, M.; Otani, Y.; Casanova, F. Unveiling the mechanisms of the spin Hall effect in Ta. *Phys. Rev. B* **2018**, *98*, 060410.

(26) Kumar, A.; Bansal, R.; Chaudhary, S.; Muduli, P. K. Large spin current generation by the spin Hall effect in mixed crystalline phase Ta thin films. *Phys. Rev. B* **2018**, *98*, 104403.

(27) Kurebayashi, H.; Sinova, J.; Fang, D.; Irvine, A. C.; Skinner, T. D.; Wunderlich, J.; Novák, V.; Campion, R. P.; Gallagher, B. L.; Vehstedt, E. K.; Zârbo, L. P.; Výborný, K.; Ferguson, A. J.; Jungwirth, T. An antidamping spin-orbit torque originating from the Berry curvature. *Nat. Nanotechnol.* **2014**, *9*, 211−217.

(28) Amin, V. P.; Stiles, M. D. Spin transport at interfaces with spin-orbit coupling: Phenomenology. *Phys. Rev. B* **2016**, *94*, 104420.

(29) Abert, C.; Sepehri-Amin, H.; Bruckner, F.; Vogler, C.; Hayashi, M.; Suess, D. Fieldlike and dampinglike spin-transfer torque in magnetic multilayers. *Phys. Rev. Appl.* **2017**, *7*, 054007.
(30) Haney, P. M.; Lee, H.-W.; Lee, K.-J.; Manchon, A.; Stiles, M. D. Current-induced torques and interfacial spin-orbit coupling. *Phys. Rev. B: Condens. Matter Mater. Phys.* **2013**, *88*, 214417.
(31) Allen, G.; Manipatruni, S.; Nikonov, D. E.; Doczy, M.; Young, I. A. Experimental demonstration of the coexistence of spin Hall and Rashba effects inβ−tantalum/ferromagnetbilayers. *Phys. Rev. B: Condens. Matter Mater. Phys.* **2015**, *91*, 144412.
(32) Kim, C.; Kim, D.; Chun, B. S.; Moon, K.-W.; Hwang, C. Evaluation Method for Fieldlike-Torque Efficiency by Modulation of the Resonance Field. *Phys. Rev. Appl.* **2018**, *9*, 054035.
(33) Tulapurkar, A. A.; Suzuki, Y.; Fukushima, A.; Kubota, H.; Maehara, H.; Tsunekawa, K.; Djayaprawira, D. D.; Watanabe, N.; Yuasa, S. Spin-torque diode effect in magnetic tunnel junctions. *Nature* **2005**, *438*, 339.
(34) Tiwari, D.; Behera, N.; Kumar, A.; Dürrenfeld, P.; Chaudhary, S.; Pandya, D. K.; Åkerman, J.; Muduli, P. K. Antidamping spin-orbit torques in epitaxial-Py(100)/β-Ta. *Appl. Phys. Lett.* **2017**, *111*, 232407.
(35) Bansal, R.; Behera, N.; Kumar, A.; Muduli, P. K. Crystalline phase dependent spin current efficiency in sputtered Ta thin films. *Appl. Phys. Lett.* **2017**, *110*, 202402.
(36) See Supplementary material.
(37) Behera, N.; Chaudhary, S.; Pandya, D. K. Anomalous anti-damping in sputtered β-Ta/Py bilayer system. *Sci. Rep.* **2016**, *6*, 19488.
(38) Colin, J. J.; Abadias, G.; Michel, A.; Jaouen, C. On the origin of the metastable β-Ta phase stabilization in tantalum sputtered thin films. *Acta Mater.* **2017**, *126*, 481−493.
(39) Liu, Q.; Zhang, Y.; Sun, L.; Miao, B.; Wang, X. R.; Ding, H. F. Influence of the spin pumping induced inverse spin Hall effect on spin-torque ferromagnetic resonance measurements. *Appl. Phys. Lett.* **2021**, *118*, 132401.
(40) Wang, Y.; Ramaswamy, R.; Yang, H. FMR-related phenomena in spintronic devices. *J. Phys. D: Appl. Phys.* **2018**, *51*, 273002.
(41) An, H.; Kanno, Y.; Asami, A.; Ando, K. Giant spin-torque generation by heavily oxidized Pt. *Phys. Rev. B* **2018**, *98*, 014401.
(42) Nan, T.; Emori, S.; Boone, C. T.; Wang, X.; Oxholm, T. M.; Jones, J. G.; Howe, B. M.; Brown, G. J.; Sun, N. X. Comparison of spin-orbit torques and spin pumping across NiFe/Pt and NiFe/Cu/Pt interfaces. *Phys. Rev. B: Condens. Matter Mater. Phys.* **2015**, *91*, 214416.
(43) Rojas-Sánchez, J.-C.; Reyren, N.; Laczkowski, P.; Savero, W.; Attané, J.-P.; Deranlot, C.; Jamet, M.; George, J.-M.; Vila, L.; Jaffrès, H. Spin Pumping and Inverse Spin Hall Effect in Platinum: The Essential Role of Spin-Memory Loss at Metallic Interfaces. *Phys. Rev. Lett.* **2014**, *112*, 106602.
(44) Yu, R.; Miao, B. F.; Sun, L.; Liu, Q.; Du, J.; Omelchenko, P.; Heinrich, B.; Wu, M.; Ding, H. F. Determination of spin Hall angle and spin diffusion length in β-phase-dominated tantalum. *Phys. Rev. Mater.* **2018**, *2*, 074406.
(45) Panda, S. N.; Mondal, S.; Sinha, J.; Choudhury, S.; Barman, A. All-optical detection of interfacial spin transparency from spin pumping in β-Ta/CoFeB thin films. *Sci. Adv.* **2019**, *5*, No. eaav7200.
(46) Chang, M.; Yun, J.; Mao, J.; Zuo, Y.; Xi, L. Effect of Inserting a Transition Metal Cu Layer on the Spin-Orbit Torque-Induced Magnetization Switching in Pt/Co/Ta Structures. *Phys. Status Solidi RRL* **2019**, *13*, 1900437.
(47) Zhu, L.; Ralph, D. C.; Buhrman, R. A. Spin-Orbit Torques in Heavy-Metal-Ferromagnet Bilayers with Varying Strengths of Interfacial Spin-Orbit Coupling. *Phys. Rev. Lett.* **2019**, *122*, 077201.
(48) Bose, A.; Singh, H.; Kushwaha, V. K.; Bhuktare, S.; Dutta, S.; Tulapurkar, A. A. Sign Reversal of Fieldlike Spin-Orbit Torque in an Ultrathin Cr/Ni Bilayer. *Phys. Rev. Appl.* **2018**, *9*, 014022.
(49) Qu, D.; Huang, S. Y.; Guo, G. Y.; Chien, C. L. Inverse spin Hall effect in Au_xTa_{1-x} alloy films. *Phys. Rev. B* **2018**, *97*, 024402.
(50) Zhu, L.; Ralph, D. C.; Buhrman, R. A. Highly Efficient Spin-Current Generation by the Spin Hall Effect in Au 1- x Pt x. *Phys. Rev. Appl.* **2018**, *10*, 031001.
(51) Pai, C.-F.; Liu, L.; Li, Y.; Tseng, H. W.; Ralph, D. C.; Buhrman, R. A. Spin transfer torque devices utilizing the giant spin Hall effect of tungsten. *Appl. Phys. Lett.* **2012**, *101*, 122404.
(52) Garello, K.; Yasin, F.; Kar, G. S. *Spin-Orbit Torque MRAM for Ultrafast Embedded Memories: From Fundamentals to Large Scale Technology Integration. 2019*; IEEE 11th International Memory Workshop (IMW), 2019; pp 1−4.
(53) Muduli, P. K.; Sharma, R.; Tiwari, D.; Sisodia, N.; Houshang, A.; Heinonen, O. G.; Åkerman, J. Microwave Oscillators and Detectors Based on Magnetic Tunnel Junctions. *Emerging Non-Volatile Memory Technologies*; Springer, 2021; pp 3−44.
(54) Fukami, S.; Anekawa, T.; Zhang, C.; Ohno, H. A spin-orbit torque switching scheme with collinear magnetic easy axis and current configuration. *Nat. Nanotechnol.* **2016**, *11*, 621−625.
(55) Vansteenkiste, A.; Leliaert, J.; Dvornik, M.; Helsen, M.; Garcia-Sanchez, F.; Van Waeyenberge, B. The design and verification of MuMax3. *AIP Adv.* **2014**, *4*, 107133.
(56) Buschow, K. H. J.; Boer, F. R. *Physics of Magnetism and Magnetic Materials*; Springer, 2003.
(57) Coey, J. M. *Magnetism and Magnetic Materials*; Cambridge University Press, 2010.
(58) Grimaldi, E.; Krizakova, V.; Sala, G.; Yasin, F.; Couet, S.; Sankar Kar, G.; Garello, K.; Gambardella, P. Single-shot dynamics of spin-orbit torque and spin transfer torque switching in three-terminal magnetic tunnel junctions. *Nat. Nanotechnol.* **2020**, *15*, 111−117.
(59) Demidov, V. E.; Urazhdin, S.; Zholud, A.; Sadovnikov, A. V.; Demokritov, S. O. Nanoconstriction-based spin-Hall nano-oscillator. *Appl. Phys. Lett.* **2014**, *105*, 172410.
(60) Slavin, A.; Tiberkevich, V. Nonlinear auto-oscillator theory of microwave generation by spin-polarized current. *IEEE Trans. Magn.* **2009**, *45*, 1875−1918.
(61) Sharma, R.; Dürrenfeld, P.; Iacocca, E.; Heinonen, O. G.; Åkerman, J.; Muduli, P. K. Mode-hopping mechanism generating colored noise in a magnetic tunnel junction based spin torque oscillator. *Appl. Phys. Lett.* **2014**, *105*, 132404.
(62) Keller, M. W.; Kos, A. B.; Silva, T. J.; Rippard, W. H.; Pufall, M. R. Time domain measurement of phase noise in a spin torque oscillator. *Appl. Phys. Lett.* **2009**, *94*, 193105.
(63) Sharma, R.; Sisodia, N.; Dürrenfeld, P.; Åkerman, J.; Muduli, P. K. Time-domain stability of parametric synchronization in a spin-torque nano-oscillator based on a magnetic tunnel junction. *Phys. Rev. B* **2017**, *96*, 024427.